The Astrophysical Journal, 1000:206 (9pp), 2026 April 1 https://doi.org/10.3847/1538-4357/ae4bd7

MHD Simulations of Strongly Magnetized H II Region Evolution: Evidence for Ionized Gas Filamentation

Samuel Crowe[1,2,3], Yisheng Tu[2,3,4], Zhi-Yun Li[2,3], Jeong-Gyu Kim[5], and John Bally[6]
[1] Oxford Centre for the History of Science, Medicine, and Technology, University of Oxford, Oxford OX2 6AH, UK; exet6431@ox.ac.uk
[2] Dept. of Astronomy, University of Virginia, Charlottesville, VA 22904, USA
[3] Virginia Institute of Theoretical Astronomy, University of Virginia, Charlottesville, VA 22904, USA
[4] Department of Astronomy, University of Michigan, Ann Arbor, MI 48103, USA
[5] Korea Institute of Advanced Study, 85 Hoegi-ro, Dongdaemun-gu, Seoul 02455, Republic of Korea
[6] Center for Astrophysics and Space Astronomy, Department of Astrophysical and Planetary Sciences, University of Colorado, Boulder, CO 80389, USA
Received 2025 November 21; revised 2026 February 23; accepted 2026 February 24; published 2026 March 24

Abstract

Recent James Webb Space Telescope observations of H II regions in the Central Molecular Zone (CMZ) have shown a highly filamentary morphology distinct from H II regions in other parts of the Galaxy. We present magnetohydrodynamic (MHD) simulations of strongly magnetized (plasma-$\beta \ll 1$) H II region evolution that investigate and describe the formation of these ionized gas filaments. H II region evolution has been simulated in a 30 pc^3 box, in distinct models with preplaced overdensities in the ambient medium and overdensities that have been generated with driven turbulence. We find that when these overdensities are seeded in the ambient medium before the birth of the ionizing source, the photoionized plasma stripped off of these dense blobs is funneled into long filaments along the magnetic field lines. The length and emission measure of these ionized gas filaments are similar to the filaments observed in the CMZ. Given that these filaments are effectively magnetically confined flows of photoionized gas, their density and curvature are influenced by the density of the blob and the geometry of the configuration.

Unified Astronomy Thesaurus concepts: H II regions (694); Galactic center (565); Radiative magnetohydrodynamics (2009); Magnetohydrodynamical simulations (1966); Interstellar filaments (842); Star formation (1569); Interstellar medium (847); Photoionization (2060)

1. Introduction

H II regions, the regions of warm, ionized gas that are typically associated with star-forming molecular clouds, stand at an important intersection in contemporary astrophysics. H II regions terminate star formation in molecular clouds before the conversion of gas to newborn stars is complete (B. Zuckerman & N. J. Evans 1974; M. Chevance et al. 2023). As signposts of star formation, particularly massive star formation, which itself has an outsized impact on the evolution of galaxies (see J. C. Tan et al. 2014; A. L. Rosen et al. 2020, for recent reviews), H II regions are crucial diagnostics of star formation rates in the Milky Way and other galaxies (R. C. Kennicutt 1989; J. P. Williams & C. F. McKee 1997; W. Lim & J. M. De Buizer 2019). Likewise, the escape of UV radiation from the H II region of a young OB association governs the interstellar and intergalactic radiation field (e.g., N. Y. Gnedin & P. Madau 2022; N. B. Linzer et al. 2024), the ionization of the diffuse interstellar medium (e.g., L. McCallum et al. 2024), and the observed dispersion measure of pulsars throughout the Galaxy (J. M. Cordes & T. J. W. Lazio 2002), among other important astrophysical processes (see also C. F. McKee & J. P. Williams 1997; L. M. Haffner et al. 2009, and references therein).

Only recently, however, has the evolution of H II regions, and their impact on star formation, been considered in more extreme regions. The Central Molecular Zone (CMZ), the central few hundred parsecs of the Milky Way (J. D. Henshaw et al. 2023), is one such region, characterized by molecular cloud densities, temperatures, turbulence, and magnetic field strengths orders of magnitude above those typically observed in the Galactic disk (see, e.g., J. Bally et al. 1987, 1988; U. Giveon et al. 2002; K. Ferrière 2009; J. M. D. Kruijssen et al. 2014; A. Ginsburg et al. 2016).

Recent James Webb Space Telescope (JWST) observations of the CMZ massive star-forming region Sagittarius C (Sgr C), at a galactocentric radius (in projection) of ∼75 pc, have revealed a striking filamentary morphology in the Sgr C H II region in the Br α hydrogen recombination line (S. Crowe et al. 2025). J. Bally et al. (2025) suggested several possible origins for the observed filaments, including supernova remnants, photodissociation regions, and fossil outflow lobes, but presented compelling evidence that a significant population of the filaments are sculpted by magnetic fields, particularly the large-scale poloidal (i.e., perpendicular to the Galactic plane) field in the CMZ.

Magnetic fields play an important role in the evolution of star-forming regions (P. Hennebelle & S.-i. Inutsuka 2019; K. Pattle & L. Fissel 2019; K. Pattle et al. 2023), and several papers have probed the effects of magnetic fields on H II region evolution in particular. M. R. Krumholz et al. (2007) and S. J. Arthur et al. (2011) found that magnetic fields inhibit H II region expansion perpendicular, but not parallel, to the field lines, producing elongated ellipsoid (rather than spherical) H II regions. L. Gendelev & M. R. Krumholz (2012) extend this treatment to "blister" H II regions, configurations where an ionizing source is positioned between a high- and low-density medium (e.g., at the edge of a dense molecular

cloud), finding that the H II region is still elongated along the magnetic field lines and that the inclusion of magnetic effects may increase the injection rate of energy into the cloud.

Finally, J. Mackey & A. J. Lim (2011) present magneto-hydrodynamic (MHD) simulations of "pillars" of neutral gas at H II region edges under uniform B-fields up to 160 μG (plasma-$\beta \sim 0.01$). When strong B-fields are included perpendicular to the pillar axis, elongated "ribbons" of ionized plasma were observed expanding perpendicular to the pillar axis (parallel to the B-field). Fields parallel to the pillar axis tended to generate "ribbons" of ionized gas extending back into the H II region, parallel to the pillar axis. The authors suggest that in highly magnetized H II regions, such filamentary structures would be readily observable in plasma tracers, such as the Br α line.

Most literature on H II region evolution in a magnetized medium considers relatively weak ($\leqslant$50 μG) fields typical of Galactic disk star-forming regions (see, e.g., C. L. Van Eck et al. 2011). The magnetic fields in the CMZ are orders of magnitude stronger than in the Galactic disk near the Sun, with CMZ field strengths ranging from 100 μG to over 1 mG in dense molecular clouds (K. Ferrière 2009). Therefore, it may be expected that magnetic fields have an outsized effect on the evolution of H II regions in highly magnetized environments like the CMZ, potentially producing the filamentation observed in Sgr C.

In this paper, we present MHD simulations of highly magnetized H II region evolution in conditions that attempt to investigate and replicate the formation mechanism of the ionized gas filaments observed in Sgr C. The paper is organized as follows. The simulation setup is described in Section 2. The results are shown and discussed in Sections 3 and 4, respectively. A conclusion is made in Section 5.

2. Methods

We present a suite of radiation magnetohydrodynamic (RMHD) simulations of H II region evolution using the grid-based code `Athena++` (J. M. Stone et al. 2020) with additional physics modules for adaptive ray-tracing and photochemistry. The additional radiation modules are largely similar to those used in J.-G. Kim et al. (2017, 2018, 2019).

The evolution of a radiatively and magnetically dominated H II region is governed by the following set of equations:

$$\frac{\partial \rho}{\partial t} + \nabla \cdot (\rho \boldsymbol{v}) = 0, \tag{1}$$

$$\frac{\partial (\rho \boldsymbol{v})}{\partial t} + \nabla \cdot \left[\rho \boldsymbol{v}\boldsymbol{v} + P^{*}\mathbb{I} - \frac{\boldsymbol{B}\boldsymbol{B}}{4\pi} \right] = \boldsymbol{f}_{\rm rad}, \tag{2}$$

$$\frac{\partial \boldsymbol{B}}{\partial t} - \nabla \times (\boldsymbol{v} \times \boldsymbol{B}) = 0, \tag{3}$$

$$\frac{\partial n_{\rm H^0}}{\partial t} + \nabla \cdot (n_{\rm H^0} \boldsymbol{v}) = \mathcal{R} - \mathcal{I}, \tag{4}$$

$$\boldsymbol{n} \cdot \nabla \boldsymbol{I} = -\chi I, \tag{5}$$

where P^{*} is the total pressure, including the gas thermal pressure and magnetic pressure, and $\boldsymbol{f}_{\rm rad}$ is the radiative force per unit volume. Instead of solving the energy equation with explicit heating and cooling terms, we adopt a simple two-temperature isothermal equation of state, used by J.-G. Kim et al. (2017), where temperature is assigned as a smoothly varying function of the fraction of neutral gas, i.e.,

$$T = T_{\rm ion} - \left(\frac{x_{\rm n}}{2 - x_{\rm n}} \right) (T_{\rm ion} - T_{\rm neu}), \tag{6}$$

where $x_{\rm n} = n_{\rm H^0}/n_{\rm H}$ is the neutral gas fraction and $T_{\rm ion} = 8000$ K and $T_{\rm neu} = 20$ K are the temperatures of the fully ionized and fully neutral gas, respectively. Since most dynamics occur in the fully ionized region, we assume the gas is in the ideal MHD limit (Equation (3)) throughout the simulation. We ignore the effects of gravity as gravity is not expected to be important in the magnetically and radiatively dominated parsec-scale environment we model. The terms on the right-hand side of Equation (4) represent creation and destruction of atomic hydrogen due to case-B radiative recombination ($\mathcal{R}$) and photoionization ($\mathcal{I}$), respectively. The remaining symbols have their usual meanings.

Photoionization is treated by solving the time-independent radiation transfer equation (Equation (5)) with photon sources representing the ionizing photons emitted by hot stars (such as O stars and B stars) in the CMZ. For the absorption coefficient per length, we adopt $\chi = n_{\rm H}\sigma_{\rm d} + n_{\rm H^0}\sigma_{\rm pi}$ with a spatially constant dust cross section of $\sigma_{\rm d} = 1 \times 10^{-21}$ cm^2 and photoionization cross section of $\sigma_{\rm pi} = 3 \times 10^{-18}$ cm^2. The hydrogen ionization fraction due to radiation is calculated with Equation (4) using a simplified photochemistry network including photoionization and recombination. Because of the high ionizing photon emission rates of the hot stars modeled in the simulation, most gas in the simulation stays either fully ionized or fully neutral, with the boundary defined by the ionization front.

We model a 30 pc^3 region with 256 cells in each direction (i.e., the resolution is 0.12 pc per cell). An ionizing source was placed at $(x, y, z) = (0, 0, 0)$ with an ionizing photon emission rate of $Q_0 = 1 \times 10^{50}$ s^{-1}, roughly corresponding to the typical ionizing photon fluxes of star-forming clouds like Sgr C (J. P. Simpson 2018). A $\hat{z}$-direction magnetic field of 1 mG was added so that the maximum plasma-β is < 1 in all regions (average $\beta \approx 10^{-5}$; in the densest regions, where n(H) $\approx 10^3$ H/cm^{-3}, $P_T/k_{\rm B} \approx 1 \times 10^7$ Kcm^{-3}, whereas $P_B/k_{\rm B} \approx 3 \times 10^8$ Kcm^{-3}). This extremely low β value means that the magnetic field changes very little in magnitude or direction across all of the simulations. The outflow boundary condition is applied at all simulation boundaries.

With the above setup, we present two models: we first illustrate one possible filament-forming mechanism using a model with artificially placed spherical overdensities in the ambient medium (hereafter referred to as "blobs"). Two blobs, each 1 pc in radius, are placed at $(x, y, z) = (5, 0, 0)$ and $(x, y, z) = (-5, 0, 5)$. The density in the blobs is uniform at 1000 H/cm^{-3}. The remaining simulation volume is filled with an ambient medium of density 100 H/cm^{-3}.

In the second model, we demonstrate how the mechanism identified in the first model naturally forms filament-like structures in a more heterogeneous initial condition where density inhomogeneities were seeded by turbulence. To generate a density inhomogeneity for our initial condition, we drive turbulence in the model for 20 Myr, with no magnetic field or ionizing source. The turbulence driving time is chosen such that the resulting density contrast is similar to the run with preset blobs. After 20 Myr, we stop the turbulence and introduce the magnetic field and ionization source.

The turbulence is driven with an energy spectrum

$$E(k) \propto k^{-2}, \tag{7}$$

where $k = 2\pi/\lambda$ is the wavenumber for a given eddy with wavelength λ. Energy was injected into the system at a rate of 2.23×10^{34} erg s^{-1}, with wavenumbers between $2 \leqslant \frac{2\pi}{\lambda} \leqslant 128$. An initial ambient density of 600 H/cm^{-3} is used to mitigate the mass loss at the simulation boundary during the driven turbulence phase. The average density of the ambient medium upon activation of the ionizing source was much lower, close to the 100 H/cm^{-3} used for the blob simulations.

3. Results

3.1. Simulation with Preplaced Blobs

Figure 1 shows various quantities of the simulation, along the x–z-plane, in the first model, with preset blobs. The first three panels, (a), (b), and (c), show cuts along the $y = 0$ plane, where the blobs are placed, of the number density, n(H), at three different times. At 0.3 Myr (b), two effects are noticeable in the blob at $z = 0$. First, the blob has begun to be compressed along the $z = 0$ plane; by 1.3 Myr (c), the blob has been flattened out into a one-dimensional stream of gas along $z = 0$. Second, this stream is comprised of largely neutral gas. Panel (d), which shows the emission measure of ionized gas along the line-of-sight, defined as

$$\mathrm{EM} = \int n_e^2 \, dl, \tag{8}$$

demonstrates this point. Much of this stream is likely made up of neutral gas from the ambient medium that is shielded from ionizing radiation by the blob rather than gas from the blob itself. Second, by 0.3 Myr, a bright, filamentary stream of dense ionized gas has formed at the tip of the blob, at $x \approx 4$ pc, about 10 pc in length. By 1.3 Myr, this filament of ionized gas has almost expanded to the length of the simulation domain ($\approx$25 pc long, see panels [c] and [d]). However, the densest (and therefore brightest) part of the filament is heavily concentrated in the innermost parsec, best seen in panel (d).

Panel (e) shows the z-velocity, v_z, with arrows showing the velocity vectors. A velocity enhancement is apparent at $x \approx 4$ pc, the location of the filament: above $z = 0$, the velocity is large and positive (around 20 km s^{-1}), and below $z = 0$, the velocity is large and negative (around -20 km s^{-1}). This implies that the filamentary structure is in fact a flow of ionized gas, rather than a static accumulation; in fact, the flow is supersonic, with Mach numbers in the range of $1.5 \sim 3$ along the length of the filament. The lower right panel shows the plasma β parameter:

$$\beta = P_T/P_B, \tag{9}$$

where P_T and P_B are the thermal and magnetic pressures, respectively. $\beta < 1$ across the entire simulation domain, implying that all of the ionized plasma is magnetically dominated. Within the ionized gas filament, β is enhanced, ranging from a few hundredths at the "tip" of the filament to $\sim$0.005 across the rest of its extent.

These last two observations—the low plasma β of the filament and its high velocity, outflowing from the tip of the neutral gas blob—imply that the filament is a magnetically confined plasma flow, a flow of ionized gas that has been stripped off (photoablated) from the surface of the dense neutral gas blob and forced to flow in line with the magnetic field in the $\hat{z}$-direction. The enhancement of β, and therefore the thermal pressure, at the tip of the blob (panel (f)), is also noteworthy, implying a negative pressure gradient out to increasing values of $|z|$ that causes the filament to expand along the direction of the magnetic field.

Interestingly, the left blob in the simulation, which is identical to the right blob except for its placement at $(x, y, z) = (-5, 0, 5)$, displays a markedly different morphology, particularly at later times. At $t = 0.3$ Myr (panel (b)), a slight density enhancement in the ionized gas can be seen on the right side of the blob as it is being photoionized, but by 1.3 Myr (panels (c), (d)), it becomes clear that the flow of plasma from this blob resembles a thick, two-dimensional "sheet" (or three-dimensional "cylinder") rather than a one-dimensional "filament." This is due to the fact that the entire bottom face of the blob is exposed to the ionizing source, meaning that the flow of ionized gas is much more extended along the x-axis than the flow of plasma from the blob at $z = 0$. The slight enhancement of thermal pressure at the tip of the blob (panel (f)) suggests that this flow of ionized plasma is indeed caused by photoionization of the outer layer of the blob, similar to the blob at $z = 0$. Clearly, the formation of a filament, in this simulation setup, depends closely on the geometry of the configuration. The $z = 0$ blob is confined and compressed by the photoevaporative flows from above and below the midplane, and the resulting filament formation is enhanced by the mirror symmetry along the z-axis, which may not be present in real clouds. Lack of symmetry about the z-axis caused the off-middle-plane blob to be pushed away together with the ambient medium, forming a corrugated surface that facilitated the formation of a "sheet" rather than a "filament." However, it is noteworthy that a curved filament-like formation is still visible in the emission measure map (panel (d)) at the ionization interface of the blob.

3.2. Simulation with Driven Turbulence

We now examine the second simulation run, where a period of driven turbulence has been used to seed an initial condition with a strong density contrast. Figure 2 shows two panels, along the x–z-plane, at the time the magnetic field and ionizing source are activated and the driving of turbulence ends (denoted as t_0, or 20 Myr). The left panel shows the total number density, n(H), in the $y = 0$ plane, and the right panel shows the column density of gas along the line of sight. As the ionizing source has just been activated, all gas is neutral at this stage. Note the large fluctuations (from $<$10 to a few $\times 10^3$ H cm^{-3}) in the ambient medium compared to the first simulation setup, which assumed a completely uniform initial density (except for the two preset spherical blobs). This creates pockets of low and high density that mirror the preset blobs considered previously.

Figure 3 shows several panels, along the x–z-plane, of the density of ionized and neutral gas at two different times after activation of the ionizing source: 0.5 and 2 Myr. Panels (a) and (b) show the total number density of gas (i.e., neutral plus ionized) along the $y = 0$ plane, whereas panels (c) and (d) show the number density of ionized gas along the $y = 0$ plane. Panels (e) and (f) show the emission measure of ionized gas along the line of sight.

At $t - t_0 = 0.5$ Myr, ionized gas filamentation is apparent in two distinct configurations (see panel [c]). Along $x \approx 2.5$ pc, a

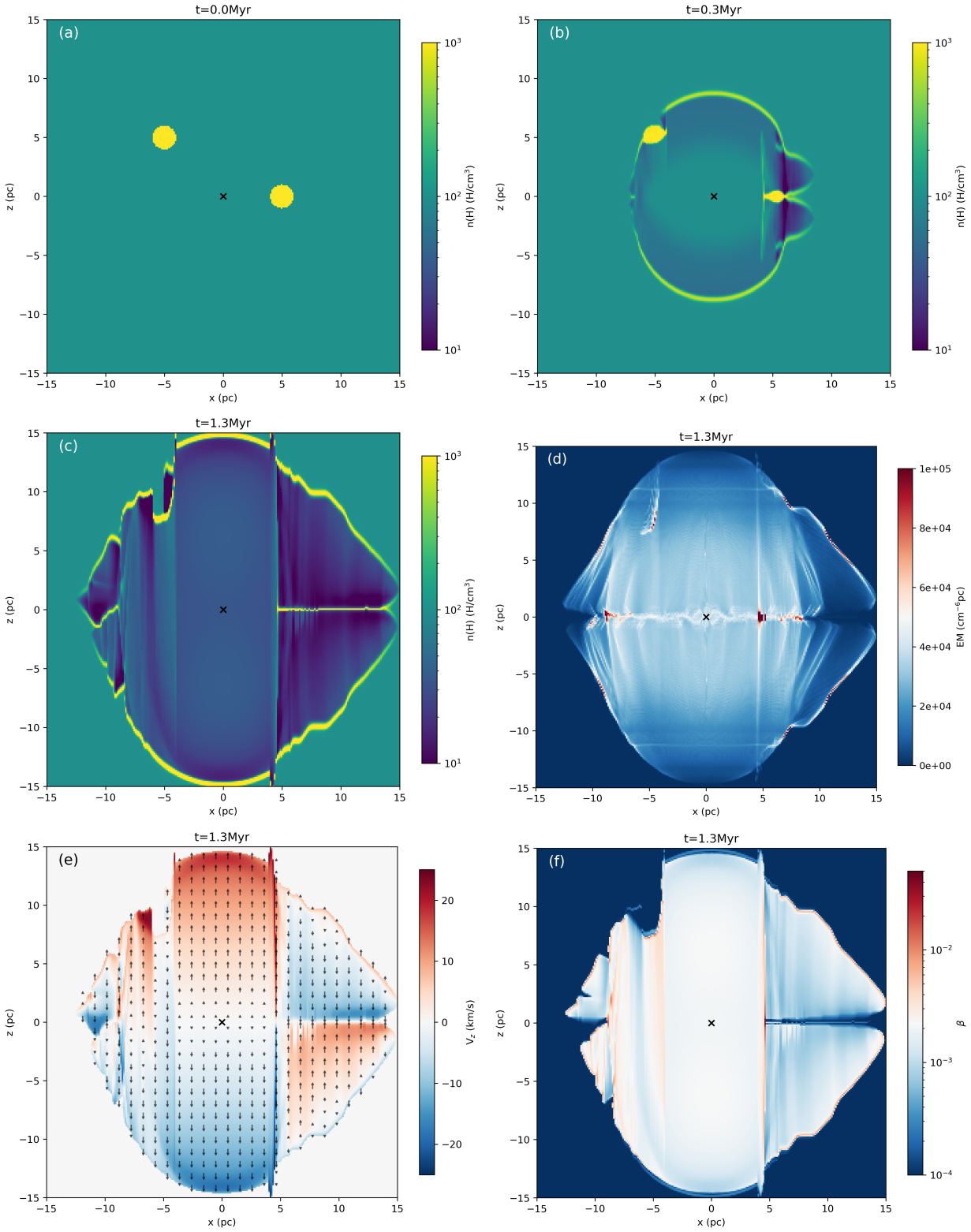

Figure 1. Select cutaways from the simulation run with preset blobs. Panel (a) shows an x–z slice (along $y = 0$) of the number density at $t = 0$, i.e., the initial condition before activation of the ionizing source. Panels (b) and (c) show the same at $t = 0.3$ and $t = 1.3$ Myr, respectively. Panel (d) shows the emission measure of ionized gas along the line of sight. Panel (e) shows the z-velocity, v_z, along an x–z slice ($y = 0$) with velocity vectors shown in black and scaled to the magnitude of the velocity. Panel (f) shows an x–z slice (along $y = 0$) of the plasma β, or thermal pressure divided by magnetic pressure. The location of the ionizing source is marked with a black cross in all panels.

dense filament extends along the z-axis, originating from the tip of a dense "pillar" of neutral gas that extends into the H II region. This ionized gas filament seems to have been generated by a similar mechanism as the filament located at $x \approx 4$ pc shown in Figure 1 and discussed in Section 3.1, with the dense "pillar" playing a nearly identical role as the dense

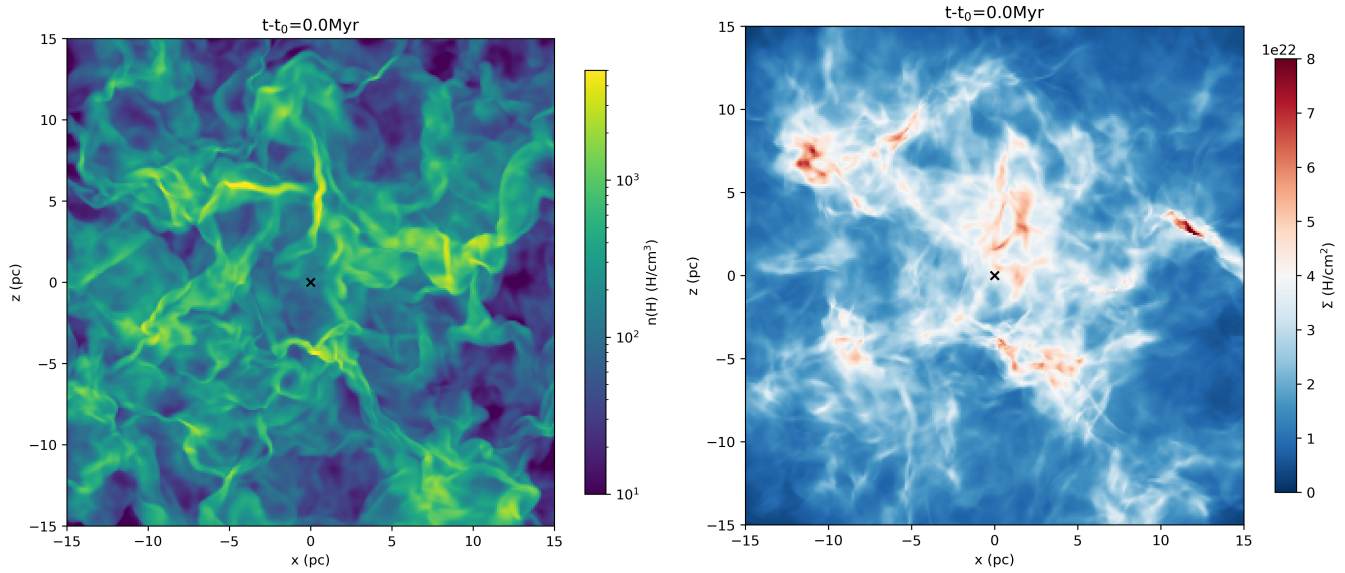

Figure 2. Gas density along the x–z-plane at the time of activation of the magnetic field and ionizing source (t_0) in the simulation run with driven turbulence. The left panel shows a slice of the gas density in the $y = 0$ plane, and the right panel shows the integrated gas density along the line of sight. The ionizing source is marked with a black cross in both panels.

blob placed at $z = 0$ in the first simulation. This filament is also apparent in the emission measure map (panel (e)) and shows the same velocity signature as shown in Figure 1 panel (e) but with Mach numbers closer to ≈1 across the filament.

Other, lower density filaments are apparent as well, including the filament (or pair of filaments) at $x \approx -4$ and $x \approx 2$ pc. These filaments do not have an obvious pillar or blob to feed them but rather are generated by specific geometries in which a "wall" of dense neutral gas at constant x is photoionized (e.g., the wall extending from $x \approx -4$, $z \approx 3 \sim 6$ pc and from $x \approx 2$, $z \approx 4 \sim 5$ pc in panel (c)), causing an overdensity of magnetically confined plasma to flow along a filament at constant x. Despite resulting from different configurations, in the underlying mechanism these two types of filaments are essentially identical: both are magnetically confined plasma flows.

At $t - t_0$=2 Myr (panels (b), (d), (f)), the H II region has evolved and expanded to the extent that several more pillars (and filaments) are apparent, including those at $(x, z) \approx (-5, -2)$, $(x, z) \approx (-6, 3)$, $(x, z) \approx (6, 7)$, $(x, z) \approx (10, -2)$, and $(x, z) \approx (11, 1)$, etc. The emission measure map, panel (f), shows a highly filamentary morphology, including filaments around the pillars mentioned above.

Many of the filaments at this time step are curved rather than almost perfectly linear like the filament in Figure 1. This can be interpreted as the result of rapid photoionization of the pillars; since essentially all of the plasma seeding a given filament comes from the tip of the pillar, as the tip retreats away from the ionizing source because of continuous photoablation, it moves across magnetic field lines, making the source of the plasma flow in the ionized filament shift across the field lines as well. For a specific illustration and explanation of this phenomenon, see the Appendix.

4. Discussion

4.1. Comparison with Sgr C

As discussed in Section 1, this study was motivated by JWST observations of ionized gas filamentation in a highly magnetized star-forming region in the CMZ, Sgr C (J. Bally et al. 2025). It must first be noted that the physical setup in the simulation is somewhat artificial and therefore not entirely representative of a real star-forming region like Sgr C. In particular, the fact that the cloud was evolved without magnetic fields, only under the effect of driven turbulence, before the input of the ionizing source and a strong (purely vertical) magnetic field, likely does not reflect the formation history of an actual CMZ cloud. Therefore, the use of our simulation to compare with Sgr C will largely be limited to the effect of strong magnetic fields on gas morphology.

The most direct comparisons can be made with the length and emission measure of the filaments in Sgr C. We choose to compare the emission measure rather than the density because of the inability to probe the line-of-sight depth of features in Sgr C and the vast differences in spatial resolution between the simulations and observations (≈0.006 pc with the JWST, 0.12 pc with our simulations). With respect to the former point, we note that the filaments in our simulations are roughly cylindrical (rather than sheet like), supporting the cylindrical approximation made in Sgr C (J. Bally et al. 2025). The latter point is more intransigent and suggests that any density derived from emission measure in the simulation would be a severe underestimate because of the overestimation of the line-of-sight depth (since $n_e \propto L^{-0.5}$).

The ionized gas filaments in Sgr C have background-subtracted emission measures ranging from a few $\times 10^4$ to $\approx 5 \times 10^5$ cm^{-6} pc, depending on the adopted extinction value, and are up to around 1 pc in length (see Table 2 of J. Bally et al. 2025). The filaments in our simulations show similar values. In the first simulation, with preplaced blobs, the brightest part of the filament at $x \approx 4$ (see Figure 1(d)) has a background-subtracted emission measure of $\approx 6 \times 10^5$ cm^{-6} pc and is around 1 pc in length, similar to the filaments in Sgr C. It is worth noting that the rest of this filament, which extends for almost the entire simulation domain, has a significantly lower emission measure, $\approx 2 \times 10^4$ cm^{-6} pc, which is below the lower end of emission measure values in Sgr C. This implies that only

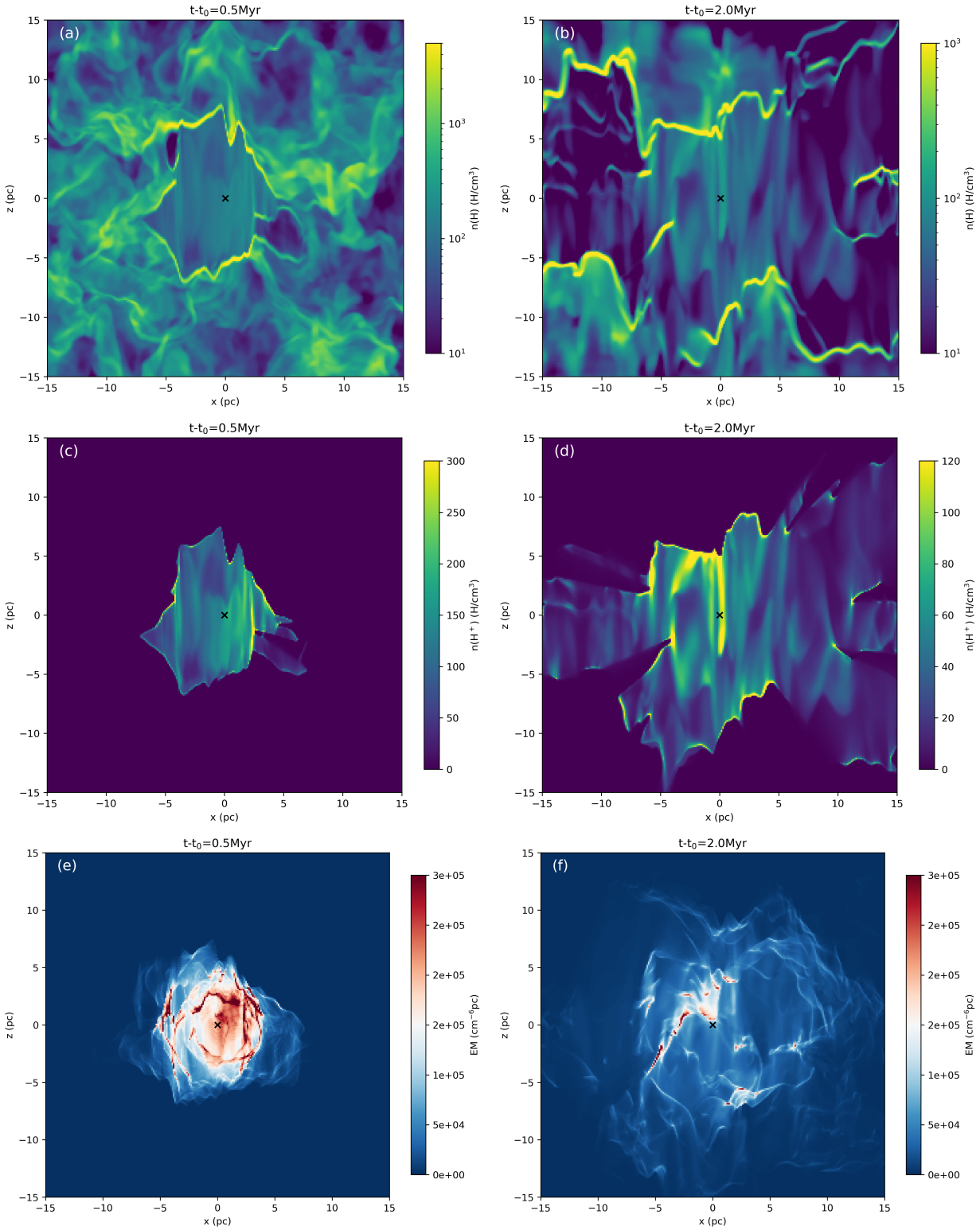

Figure 3. Select cutaways from the simulation run with driven turbulence. Panels (a) and (b) show x–z slices (along $y = 0$) of the total number density of gas at $t - t_0 = 0.5$ and 2 Myr, respectively. Panels (c) and (d) show the same but for the ionized gas number density. Panels (e) and (f) show the emission measure of ionized gas along the line of sight. The location of the ionizing source is marked with a black cross in all panels.

the innermost parsec of this filament would be visible in Sgr C. Inversely, this result suggests that the filaments in Sgr C may in fact be much longer than were observed simply due to the sensitivity limits of the JWST observations. The filaments in the simulation run with driven turbulence also show a similar emission measure to the filaments in Sgr C.

The shape, extent, and age of the simulated H II region and Sgr C are also worth comparing. The "core" of the brightest

emission in the Sgr C H II region measures around 7 pc on its long dimension (roughly parallel to the Galactic plane) and around 5 pc on its short dimension (perpendicular to the Galactic plane). The "core" of the most dense portion of the simulated H II region is around 10 pc in all dimensions, or about twice as large as Sgr C, although there is some slight preferential elongation along the *x*- and *y*-axes at later times (see panels (d), (f) of Figure 3). The $\approx 2\times$ difference in overall size may be attributable to the $\approx 2\times$ higher average density in Sgr C compared to the simulated medium, though many other factors may be at play.

There are some striking similarities in the shape of the two H II regions. As mentioned, both the simulated and observed H II regions are nearly spherical (circular in the case of Sgr C) but slightly elongated perpendicular to the magnetic field lines (if, in the case of Sgr C, the poloidal component of the CMZ magnetic field is the dominant one, which is tenuously suggested by the statistical preference of filament orientations along the poloidal component of the field; see Figure 6 of J. Bally et al. 2025). This result is quite unexpected given the suggestion of several previous studies that simulated magnetized H II regions are distorted and elongated parallel to the field lines (M. R. Krumholz et al. 2007; S. J. Arthur et al. 2011; M. Zamora-Avilés et al. 2019; L. Gendelev & M. R. Krumholz 2012). It is possible that this phenomenon, the elongation of the H II region perpendicular to the field, could be due to the lifting of material away from the midplane by the strong perpendicular magnetic field, allowing the ionizing radiation to cleave through regions of higher density more easily and carve out a lower density "tunnel" along the midplane (see panels (b), (d) of Figure 3). However, this is only one possible mechanism.

Another interesting feature is the presence of a diffuse, filamentary "halo" of ionized gas around the "core" of the H II region, which is seen in both Sgr C and the simulation. This is best seen in panel (f) of Figure 3 and the top panel of Figure 4 of J. Bally et al. (2025). This diffuse halo implies leakage of ionizing photons into the extended medium surrounding each H II region; in the case of the simulation with driven turbulence, this is likely due to the ease with which the ionization front eats through regions of low density, forming the pockets of ionized gas best seen in panel (d) of Figure 3.

Finally, one interesting comparison between the filaments in Sgr C and the simulated H II region is the morphology of the filaments themselves. The filaments in Sgr C are generally more numerous and have a wider diversity of curvature and orientation than the filaments in the simulated H II region. Both differences (particularly in number of filaments) are likely attributable in large part to discrepancies in resolution between the observations and simulation. Differences in curvature are likely due to lower density in the blob/pillar/wall that feeds the filament, causing the source of the plasma flow to shift as the reservoir of neutral gas is rapidly eroded away; this is explored further in the Appendix. Differences in orientation are harder to treat as they imply complicated line-of-sight effects in Sgr C that are difficult to model with the constraints on resolution and magnetic field orientation in the simulation setup used in this work. Particularly, the filamentation in Sgr C often displays a pattern of overlapping or nearly overlapping filaments with different orientations, at times even in a cross-hatching pattern (see Figure 5 and Appendix A of J. Bally et al. 2025). This implies locally varying magnetic fields, both across the plane of the sky and along the line of sight, that have been suggested in the literature (see, e.g., R. G. Tress et al. 2024) and are not modeled in the simulations presented in this paper. Future high-resolution mapping of the magnetic field in magnetically dominated H II regions, like Sgr C, may further illuminate the effect on local magnetic field variation on filament formation.

Also important are measurements of the velocity of the ionized gas, since the model for filament formation given in the present study rests on the motion of the ionized gas, particularly at speeds that meet or exceed the sound speed. Therefore, high spatial- and velocity-resolution observations of the ionized gas in Sgr C, and other CMZ H II regions, will be crucial to testing our model. Acceleration of the ionized gas may be an important consequence of the incorporation of magnetic fields into H II region models and contribute to the surprisingly high velocities observed in some H II region complexes (e.g., Orion, C. Pabst et al. 2019).

5. Conclusions

In this paper, we have presented a suite of RMHD simulations of H II region expansion and evolution that effectively demonstrates the formation of ionized gas filaments in strong magnetic fields. We find that these filaments can be explained effectively as magnetically confined ($\beta \ll 1$) flows of photoionized plasma. These flows must be seeded by a reservoir of dense neutral gas. We present two possible geometries, one in which the reservoir is a freestanding dense "pillar" or "blob" and one in which the reservoir is a long "wall" of neutral gas parallel to the magnetic field. In both cases, the curvature of the filament is dependent on the density of the reservoir.

A key feature of our model for ionized gas filament formation is the motion of the ionized gas. In particular, we predict relatively high velocities, around a few dozen kilometers per second, within the filaments. Therefore, future high spatial and velocity measurements of ionized gas in highly magnetized H II regions will be crucial to testing our model.

We find a favorable comparison between the length and emission measure of the simulated filaments and the filaments in Sgr C. We also observe a slight elongation of the simulated H II regions perpendicular to the field lines that may also be present in Sgr C.

However, we are not able to replicate the large number and diversity of filament orientations observed in Sgr C and the complicated structure along the line of sight. We expect that this will be more difficult to treat, involving greater knowledge of the local magnetic field in highly magnetized H II regions like Sgr C and more sophisticated, higher-resolution simulations accounting for rapid variations in the local magnetic field.

Acknowledgments

This work is based on simulations performed using computing resources from UVA research computing (RIVANNA) and NSF's ACCESS computing allocation PHY250098. S.T.C. acknowledges support from the award JWST-GO-04147.003-A. Y.T. acknowledges support from the interdisciplinary fellowship at UVA. Z.Y.L. and Y.T. are

supported in part by NASA 80NSSC20K0533, NSF AST-2307199, JWST-GO-02104.002-A, and the Virginia Institute of Theoretical Astronomy (VITA). J.-G.K acknowledges support from KIAS Individual Grant QP098701 at Korea Institute for Advanced Study.

Appendix
Model with Lower Blob Densities: Curved Filaments

In order to demonstrate the mechanism by which a curved ionized gas filament, discussed in Section 3.2, could form, we present a model with identical setup to the preset blob simulation described in Section 2 but with blob densities of 250 $\mathrm{H/cm^{-3}}$ rather than 1000 $\mathrm{H/cm^{-3}}$, i.e., 4 $\times$ lower, only 2.5 $\times$ more dense than the ambient medium.

The results are presented in Figure 4 (similar to Figure 1). Panel (a) shows the number density, n(H), on an x–z slice along $y = 0$, at $t = 0$, i.e., the initial condition. Panel (b) shows the same at $t = 1.3$ Myr. It can be seen that, in contrast to the filament in panel (b) of Figure 1, this filament (density enhancement) displays a curved morphology, which is reinforced by the ionized gas emission measure shown in panel (c) and velocity plot shown in panel (d). This effect can be explained by the lower density of the neutral gas reservoir, which causes a more rapid depletion of neutral gas as the ionization proceeds. Because the filament (ionized gas flow) is sourced at the "tip" of the neutral gas reservoir, the rapid erosion of the "tip" means that as ionization proceeds, separate, connected channels of ionized gas, at different x-values, are created, giving the appearance of a curved filament even though the plasma is still constrained to flow along the local field lines. A similar mechanism could be invoked to justify the presence of curved filaments in highly magnetized H II regions like Sgr C.

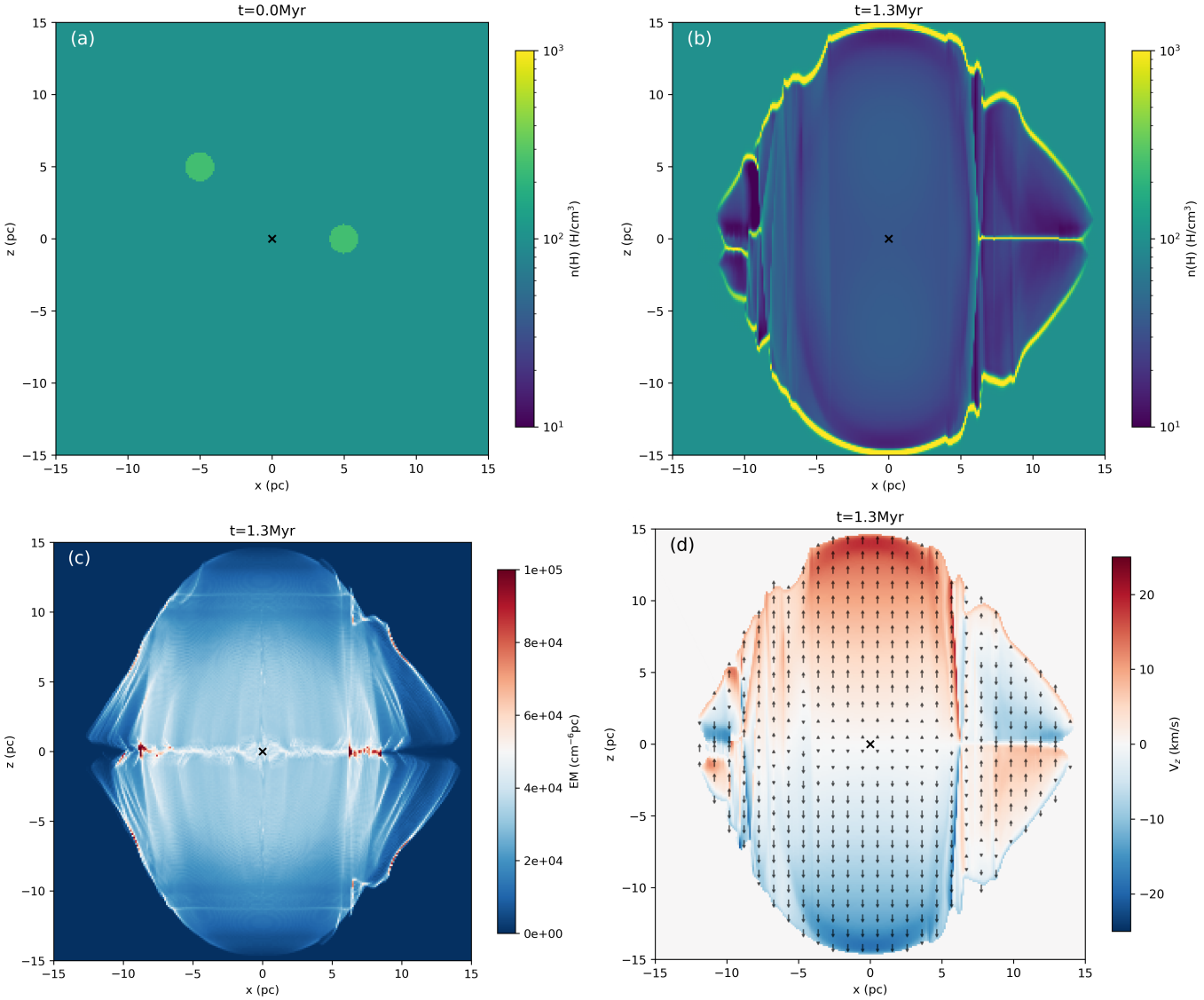

Figure 4. Cutaways from a simulation run with preset blobs of lower density than presented in Section 3.1 and Figure 1. Panel (a) shows an x–z slice (along $y = 0$) of the number density at $t = 0$, i.e., the initial condition before activation of the ionizing source. Panel (b) shows the same at $t = 1.3$ Myr. Panel (c) shows the ionized gas emission measure along the line of sight. Panel (d) shows the the z-velocity, v_z, along an x–z slice ($y = 0$) with velocity vectors shown in black and scaled to the magnitude of the velocity. The location of the ionizing source is marked with a black cross in all panels.

ORCID iDs

Samuel Crowe https://orcid.org/0009-0005-0394-3754
Yisheng Tu https://orcid.org/0000-0003-2929-1502
Zhi-Yun Li https://orcid.org/0000-0002-7402-6487
Jeong-Gyu Kim https://orcid.org/0000-0001-6228-8634
John Bally https://orcid.org/0000-0001-8135-6612

References

Arthur, S. J., Henney, W. J., Mellema, G., de Colle, F., & Vázquez-Semadeni, E. 2011, MNRAS, 414, 1747
Bally, J., Stark, A. A., Wilson, R. W., & Henkel, C. 1987, ApJS, 65, 13
Bally, J., Stark, A. A., Wilson, R. W., & Henkel, C. 1988, ApJ, 324, 223
Bally, J., Crowe, S., Fedriani, R., et al. 2025, ApJ, 983, 20
Chevance, M., Krumholz, M. R., McLeod, A. F., et al. 2023, ASPC, 534, 1
Cordes, J. M., & Lazio, T. J. W. 2002, arXiv:astro-ph/0207156
Crowe, S., Fedriani, R., Tan, J. C., et al. 2025, ApJ, 983, 19
Ferrière, K. 2009, A&A, 505, 1183
Gendelev, L., & Krumholz, M. R. 2012, ApJ, 745, 158
Ginsburg, A., Henkel, C., Ao, Y., et al. 2016, A&A, 586, A50
Giveon, U., Sternberg, A., Lutz, D., Feuchtgruber, H., & Pauldrach, A. W. A. 2002, ApJ, 566, 880
Gnedin, N. Y., & Madau, P. 2022, LRCA, 8, 3
Haffner, L. M., Dettmar, R.-J., Beckman, J. E., et al. 2009, RvMP, 81, 969
Hennebelle, P., & Inutsuka, S.-i. 2019, FrASS, 6, 5
Henshaw, J. D., Barnes, A. T., Battersby, C., et al. 2023, ASPC, 534, 83
Kennicutt, R. C., Jr. 1989, ApJ, 344, 685
Kim, J.-G., Kim, W.-T., & Ostriker, E. C. 2018, ApJ, 859, 68
Kim, J.-G., Kim, W.-T., & Ostriker, E. C. 2019, ApJ, 883, 102
Kim, J.-G., Kim, W.-T., Ostriker, E. C., & Skinner, M. A. 2017, ApJ, 851, 93
Kruijssen, J. M. D., Longmore, S. N., Elmegreen, B. G., et al. 2014, MNRAS, 440, 3370
Krumholz, M. R., Stone, J. M., & Gardiner, T. A. 2007, ApJ, 671, 518
Lim, W., & De Buizer, J. M. 2019, ApJ, 873, 51
Linzer, N. B., Kim, J.-G., Kim, C.-G., & Ostriker, E. C. 2024, ApJ, 975, 173
Mackey, J., & Lim, A. J. 2011, MNRAS, 412, 2079
McCallum, L., Wood, K., Benjamin, R., et al. 2024, MNRAS, 530, 2548
McKee, C. F., & Williams, J. P. 1997, ApJ, 476, 144
Pabst, C., Higgins, R., Goicoechea, J. R., et al. 2019, Natur, 565, 618
Pattle, K., & Fissel, L. 2019, FrASS, 6, 15
Pattle, K., Fissel, L., Tahani, M., Liu, T., & Ntormousi, E. 2023, ASPC, 534, 193
Rosen, A. L., Offner, S. S. R., Sadavoy, S. I., et al. 2020, SSRv, 216, 62
Simpson, J. P. 2018, ApJ, 857, 59
Stone, J. M., Tomida, K., White, C. J., & Felker, K. G. 2020, ApJS, 249, 4
Tan, J. C., Beltrán, M. T., Caselli, P., et al. 2014, Protostars and Planets VI (Univ. Arizona Press), 149
Tress, R. G., Sormani, M. C., Girichidis, P., et al. 2024, A&A, 691, A303
Van Eck, C. L., Brown, J. C., Stil, J. M., et al. 2011, ApJ, 728, 97
Williams, J. P., & McKee, C. F. 1997, ApJ, 476, 166
Zamora-Avilés, M., Vázquez-Semadeni, E., González, R. F., et al. 2019, MNRAS, 487, 2200
Zuckerman, B., & Evans, N. J., II 1974, ApJL, 192, L149